A Full-Wave Helmholtz Model for Continuous-Wave Ultrasound Transmission

Tomi Huttunen, Matti Malinen, Jari P. Kaipio, Phillip Jason White, Kullervo Hynynen

Abstract

A full-wave Helmholtz model of continuous-wave (CW) ultrasound fields may offer several attractive features over widely used partial-wave approximations. For example, many full-wave techniques can be easily adjusted for complex geometries and multiple reflections of sound are automatically taken into account in the model. To date, however, the full-wave modeling of CW fields in general 3D geometries has been avoided due to large computational cost associated with the numerical approximation of the Helmholtz equation. Recent developments in computing capacity together with improvements in finite element type modeling techniques are making possible wave simulations in 3D geometries which reach over tens of wavelengths. The aim of this study is to investigate the feasibility of a full-wave solution of the 3D Helmholtz equation for modeling of continuous-wave ultrasound fields in an inhomogeneous medium. The numerical approximation of the Helmholtz equation is computed using the ultra weak variational formulation (UWVF) method. In addition, an inverse problem technique is utilized to reconstruct the velocity distribution on the transducer which is used to model the sound source in the UWVF scheme.

The modeling method is verified by comparing simulated and measured fields in the case of transmission of 531 kHz CW fields through layered plastic plates. The comparison shows a reasonable agreement between simulations and measurements at low angles of incidence but due to mode conversion, the Helmholtz model becomes insufficient for simulating ultrasound fields in plates at large angles of incidence.

I. INTRODUCTION

A full-wave Helmholtz model may offer several attractive features over commonly used partial wave and time-domain approximations. For example, multiple reflections and standing waves are automatically taken into account in the model. And a full-wave Helmholtz method that uses finite element meshes can be more easily adjusted for a general geometry and medium [1]. Due to large computer requirements,

T. Huttunen, M. Malinen and J.P. Kaipio are with the Department of Applied Physics, University of Kuopio, Finland

P.J. White and K. Hynynen are with the Brigham and Women’s Hospital, Harvard Medical School

however, a full-wave Helmholtz modeling of practical 3D ultrasound problems is considered too time-consuming [2], [3]. Conventional numerical methods, such as low-order finite difference and finite element methods, suffer from the need of extremely dense spatial discretization and lead to overwhelmingly large computational tasks. Therefore, large-scale ultrasound fields are commonly modeled using different kinds of ray approximation [2]–[5] or projection methods [6]–[11].

These methods are accurate and effective if the propagation medium is rather simple and multiple reflections do not occur. For example in [5] a ray method and in [8], [11] projection methods are successfully applied to ultrasound through layered media. However, the efficiency of the partial wave approximations may be limited in complex geometries and strongly scattering media; or if waves undergo complex interference phenomena. In particular, in the case of continuous-wave fields in inhomogeneous media, multiple reflections can produce complex standing wave patterns which are not easy to capture using the partial wave methods. Hence, although fast in a relatively simple medium and geometry, ray-tracing and projection methods may become difficult and time-consuming for continuous-wave ultrasound problems in general geometries.

An alternative approach for modeling ultrasound fields has been the use of full-wave time-domain methods, such as the finite difference time-domain (FDTD) method. For continuous-wave problems, a time-domain method requires a large number of time steps (in addition to a dense spatial discretization) to reach a steady-state solution [12]. This also leads to a heavy computational burden and hence, various improved time-domain methods for relaxing the mesh density requirement of wave problems have been proposed. The methods that need few number of grid point per wavelength include the k-space method [13], [14], pseudospectral methods [15]–[17] and spectral element methods [18].

Although very promising results are reported for the feasibility of the k-space method for large-scale modeling of ultrasound pulses in weakly inhomogeneous tissues, the applicability of the method for strongly scattering media is not known yet. Pseudospectral and spectral element methods can be used for problems in strongly heterogeneous media but they also need a large number of time step to approximate CW fields. Therefore, despite the recent improvements, realistic 3D applications of time-domain methods for continuous-wave problems are still computationally extremely demanding.

The rapid development of computing capacity accompanied with recent improvements in full-wave solution techniques have started to enable simulations of realistic 3D ultrasound problems using the Helmholtz model. A review of numerical methods for the Helmholtz equation is presented in Section II. In this study, a full-wave approximation of the Helmholtz equation is used for modeling ultrasound fields in inhomogeneous media. The Helmholtz equation is solved using the ultra weak variational formulation (UWVF) [19]–[22] in geometries consisting of layered structures. To reduce the numerical reflections due to truncation of the computational domain, the UWVF method is coupled with the perfectly matched layer (PML) [23]. The simulation tool used in this study is essentially the same that was introduced in [24] so only a short outline of the method is given in Section II.

II. NUMERICAL APPROXIMATION OF THE HELMHOLTZ EQUATION

In this section, the Helmholtz model is introduced and methods for its numerical approximation are reviewed. Let $r = (x, y, z)$ denote the spatial variable. A linear time-dependent pressure field in an inhomogeneous fluid with the spatially varying speed of sound $c = c(r)$ and density $\rho = \rho(r)$ can be modeled using the wave equation [25]

$$\rho \nabla \cdot \left(\frac{1}{\rho} \nabla P \right) - \frac{1}{c^2} \frac{\partial^2 P}{\partial t^2} = 0. \tag{1}$$

For continuous-waves $P(r,t) = p(r)e^{-i\omega t}$, the wave equation (1) for the spatially dependent part p reduces to the Helmholtz equation

$$\nabla \cdot \left(\frac{1}{\rho} \nabla p \right) + \frac{\kappa^2}{\rho} p = 0, \tag{2}$$

where $\kappa = \omega / c(r) + i\alpha(r)$ is the wave number and $\omega = 2\pi f$ is the angular frequency. In this form, the absorption can be taken into account using complex valued wave numbers where $\alpha(r)$ is the absorption coefficient.

Three commonly used methods to approximate the Helmholtz equation (2) in a medium with strong inhomogeneities are finite difference methods [26], finite element methods [27] and boundary integral methods [28]. Finite difference and finite element methods rely on the discretization of the volume of interest and therefore allow, at least in principle, an arbitrary variation of the material parameters within the computational domain. On the other hand, if the medium consists of piecewise constant materials, it is possible to apply the Kirchhoff-Helmholtz integral theorem [25] and rewrite the Helmholtz problem using boundary integrals over material interfaces only.

In a finite difference method, the region of interest is covered with a discrete set of points at which the pressure field is coupled with the pressure at adjacent points via discrete approximations for differential operators [26]. For a typical finite element method, the computational domain is partitioned into a finite number of small elements in which the pressure field is approximated using low-order polynomials [27]. While finite difference and finite element methods have been successful in wave problems at low wave numbers, they become overwhelmingly complex at high wave numbers. The reason for this is twofold. First, *a rule of thumb* for both methods states that the density of the discretization points should be ten points per wavelength in order to achieve a tolerable accuracy (i.e. $\lambda/h \approx 10$ where λ is the wavelength and h is the side length of a finite element or the distance between adjacent finite difference points). Second, the density of discretization points per wavelength must increase with the wave number to maintain accuracy on a fixed level. The latter is due to phenomenon called *numerical pollution* [27].

The error of the 1D and 2D piecewise linear finite element approximations of the Helmholtz problem is investigated in [27]. The results suggest that the rule of thumb is not sufficient to obtain a small error at high wave numbers. Instead, in a 1D model problem, the error remained on a fixed level when $\kappa^3 h^2$ is constrained. The numerical pollution of the finite element method is also observed in 2D and 3D simulations [29], [30]. However, the effect of the pollution can be reduced, and thus the requirement of the mesh density can be relaxed, by using alternative finite element formulations [30].

Various discretization methods for the boundary integral formulations of the Helmholtz problem have been proposed. These include, for example, the Nyström method [31], collocation method [32] and different types of Galerkin boundary element methods [28]. Although with the use of these methods, the density of discretization points can be slightly relaxed, the boundary integral methods still lead to heavy computations at high wave numbers, mainly since the resulting matrix equations are full. Another drawback is that the boundary integral approach leads to an increasingly complex system of coupled integral equations if the number of inhomogeneities within the computational domain increases.

In a computational cost comparison, the boundary element methods have been shown to be more expensive than a low-order finite element method [33], [34]. Particularly, the solving of boundary integral equations with iterative solvers necessitates the computation of multiple full matrix-vector products. Fortunately, this procedure can be accelerated by using the fast multipole method (FMM), see e.g. [35]–[37]. Improved by the FMM, boundary integral equations offer an efficient means for solving large-scale scattering problems [36].

A relatively new development in the reducing of computational burden for finite element type methods has been the use of basis functions that are tailored for wave problems. In the partition of unity finite element method (PUM) [38], [39], conventional piecewise linear basis functions are multiplied by plane waves. These new basis functions better imitate the oscillatory nature of the solution of the Helmholtz problems and relax the rule of thumb for the element size. Similarly, *a priori* information of the solution (in the form of plane wave basis functions) has been included in the approximating functions in the least-squares method [40], discontinuous enrichment method [41], discontinuous Galerkin method [42] and ultra weak variational formulation [19]–[22], [24], [43],

The general form of the ultra weak variational formulation (UWVF) was first introduced in [19]. Subsequently, the method was analyzed for the Helmholtz and Maxwell equation in 2D and 3D [20]–[22]; and 2D Navier equation in [44]. In addition, [20] includes the formulation of the UWVF for the Helmholtz problem in an inhomogeneous medium.

The idea of the UWVF is to decompose the original problem into a set of subproblems which are connected using a coupled boundary condition which characterizes the continuity of acoustic pressure and normal particle velocity across element interfaces. For the geometric partition of the computational domain, the UWVF uses standard disjoint finite element meshes, so that each element of the mesh determines a single subproblem for the UWVF. By setting the material properties for each element to be constant, the approximating space for the discrete UWVF can be constructed using free-space solutions of each subproblem. In practice, the discrete UWVF approximation of the pressure field in a single element is constructed as a weighted sum of plane waves. The discretization of the UWVF leads to a matrix equation from which the weights can be computed.

In its original form, the UWVF method may suffer from numerical instability. A more stabilized method for choosing the basis functions has been proposed in [43]. Simulations for 2D elastic wave propagation showed that the UWVF reduces the overall memory requirement compared to a low-order finite element method [44].

There is, however, an additional challenge in the full-wave modeling which must be take into account while building the model. This is the truncation of computational domain without spurious numerical reflections. More precisely, many ultrasound experiments are conducted in a relatively large water tank in which only a small volume constitutes the region of interest. To avoid an unnecessarily large computational domain, the region of interest can be enclosed by an artificial boundary on which an *absorbing boundary condition* (ABC) can be used to imitate the outgoing behavior of the wave field. The classical approach in FEM for constructing an ABC has been the use of differential or integro-differential operators [45]. A low-order (Sommerfeld-type) differential operator has been used with the UWVF in [21], [43], [46]. Alternatively, the region of interest can be surrounded by a computational sponge layer called the *perfectly matched layer* (PML) [23]. The UWVF-PML method used in this study is analyzed more detailed in [24].

III. INVERSE PROBLEM FOR THE VELOCITY DISTRIBUTION

A crucial issue in the simulation of ultrasound fields emitted by a transducer is the proper modeling of the velocity distribution on the transducer. Fields emitted by an oscillating surface with the uniform normal velocity distribution are widely used in theoretical acoustics but they are rarely sufficient for modeling fields from real ultrasound transducers. In [47], experimentally measured fields from the polyvinylidene fluoride (PVDF) and lead zirconate titanate (PZT) transducers were compared with theoretical models. They observed that PVDF sources had a good agreement with the model that assumed the uniform velocity distribution on the transducer. However, in the case of the PZT elements, marked amplitude variations on the transducer were found. A notable variation in the amplitude and phase of transducers surface velocity pattern of CW sources was also observed in [48].

Since the experimental measurements of this study are conducted using PZT elements, the model must take into account the specific velocity pattern of the transducer. Typically, the surface velocity is reconstructed from the measurements that are made in a plane parallel to the transducers surface in the front of the transducer. In the projection methods [6], [9], [48], the measured field is Fourier transformed and the field can be easily projected backward to the source plane. The pressure field in that plane can be resolved using the inverse Fourier transform.

In the equivalent phased array method (EPAM), the transducer is assumed to consist of a “phased array” of small elements [49]. Each element oscillates with its own amplitude and phase. Then, the field in the measurement plane is obtained as a discrete Rayleigh integral over the fictitious elements. As will be shown later, the pressure field in the measurement plane can be written in the form of the matrix equation in which the vector of complex valued velocities for each element is multiplied by a matrix arising from the discrete Rayleigh integral. Obviously, if the pressure field is known, the velocity vector can be obtained as the inverse of the same matrix. In the EPAM, the inversion of the system matrix is computed as the pseudo-inverse which produces the minimum norm solution for the source. A similar technique was first introduced to predict driving amplitudes and phases of phased arrays for ultrasound hyperthermia [50], [51].

The surface velocities obtained from both methods have been shown to lead to a reliable reconstruction of the pressure field if rather strict measurement conditions are fulfilled. Namely, the field must be measured with relatively dense spacing and the measurement plane must be large enough to contain sufficient amount of information of the pressure field.

As was noted in [49], the surface velocity distribution obtained via the EPAM is not the same as the real particle velocity. Rather, the method gives the excitation source which produces a similar acoustic field as the measured one. The EPAM method is also sensitive to the input pressure field, that is, pressure data from different measurement planes may lead to different velocity distribution.

From the methodological point of view, the source reconstruction belongs to the class of *inverse problems*. In the forward problem, the task is to resolve the resulting pressure fields from the known surface velocity distribution. Consequently, the inverse problem can be defined as finding the sound source if the pressure field (or a part of it) is known. Particularly since a small variation in the measured pressure data may result in large changes in the surface velocity, the inverse problem is said to be *ill-posed*. A common property of ill-posed problems is that the system matrix is ill-conditioned. Standard techniques for treating the ill-conditioned inverse problems are discussed for example in [52]. Typically, the ill-conditioned problem is replaced with a nearby well-posed problem. Hence, the problem is said to be regularized.

The inverse problem approach for the acoustic source reconstruction has been used for example in [53]. In that study the aim was to reconstruct the source of a tire noise. Due to the complex geometry of the tire, the forward modeling was made using the boundary element method (BEM). The inverse problem was solved with *Tikhonov regularization*.

The formulation of the forward problem in this study is the same as in the equivalent phased array method. However, to relax the restrictions of the measurement conditions, a similar regularization technique as in [53] is used to invert the matrix equation.

Assuming that the surface of the transducer S consists of finite sized elements $S = \cup_{j=1}^{N} dS_j$, the discrete Rayleigh integral for the pressure at point $r = (x, y, z)$ can be written as

$$p(r) = \sum_{j=1}^{N} v_{n,j} \left(\frac{i\omega\rho}{2\pi} \frac{e^{i\kappa|r-r_j|}}{|r-r_j|} dS_j \right), \tag{3}$$

where r_j is the centroid of the element dS_j and $v_{n,j}$ is the normal velocity at the point r_j.

Let the field be measured at points $r_m, 1 \leq m \leq M$. Then, the pressure field in the measurement points $p(r_m) = p_m$ can be solved from the matrix equation

$$p = Hv_n,$$

where

$$p = \begin{pmatrix} p_1 \\ p_2 \\ \vdots \\ p_M \end{pmatrix}, \quad H = \begin{pmatrix} h_{1,1} & h_{1,2} & \dots & h_{1,N} \\ h_{2,1} & h_{2,2} & \dots & h_{2,N} \\ \vdots & \vdots & \ddots & \vdots \\ h_{M,1} & h_{M,2} & \dots & h_{M,N} \end{pmatrix}$$

and

$$v_n = \begin{pmatrix} v_{n,1} \\ v_{n,2} \\ \vdots \\ v_{n,N} \end{pmatrix};$$

and where

$$h_{m,j} = \frac{i\omega\rho}{2\pi} \frac{e^{i\kappa|r_m - r_j|}}{|r_m - r_j|} dS_j.$$

The discrete approximation is accurate if the size of the elements dS_j is small compared to the wavelength. Typically, at least two elements per wavelength are needed for tolerable accuracy.

In the equivalent phased array method [49], the velocity distribution on the transducer is obtained using the pseudo-inverse of the matrix H. As noted earlier, this produces the minimum norm solution for the velocity v_n which can be different from the real velocity distribution. Therefore, in this study, a Tikhonov regularization [54] is used. Hence, the velocity vector v_n is obtained as the solution of the equation

$$v_n = (H^*H + \gamma^2 I)^{-1} H^* p, \tag{4}$$

where H^* refers to conjugated transpose of the matrix H and γ is the so-called regularization parameter.

IV. MEASUREMENT SETUP

The experimental measurements discussed next have two aims. On one hand, the measured data is needed to reconstruct the velocity distribution on the transducer. The estimated velocity is used for the realistic modeling of the source in the transmission simulations. On the other hand, the measurements of the transmitted fields for the plastic targets are required for the forthcoming comparison with the simulated results.

Experiments are conducted in a tank filled with deionized and degassed water. The walls of the tank are padded with rubber to prevent spurious reflections. A schematic illustration of the experimental setup is presented in Fig. 1.

[Figure 1 about here.]

The 30 mm diameter circular planar transducer is made of PZT-4 and it is operated at frequency $f = 531$ kHz. The sinusoidal transducer signal is generated with a waveform generator (Wavetek 395, USA) and amplified with a power amplifier (ENI A150, Rochester, NY, USA). A power meter (Agilent E4419E, Palo Alto, CA, USA) is used to monitor the input power of the transducer. The angle of plastic layers in the front of the transducer are controlled with a motor driven rotary table (Velmex, Bloomfield, NY, USA).

Two types of layered plastic plates are used. Plate 1 is a single layer (thickness 11.8 mm) of plastic 1 and Plate 2 consists of a 6.0 mm thick layer of rubber sandwiched between two 3.1 mm thick plates of plastic 2. The material properties of the plastic used for the plates and water are listed in Table I. All properties were measured in-house, except the absorption coefficients for polycarbonate and plexiglas from [55] were used for plastic 1 and plastic 2, respectively.

[Table 1 about here.]

The transmitted field is measured using a 0.2 mm diameter PVDF needle hydrophone (Precision Acoustics SN762, Dorchester-Dorset, UK). Simulations in [46] showed that the diameter of the needle is small enough for avoiding standing waves between the transducer and the needle. The hydrophone is moved in the tank using a a stepping motor controlled 3D positioning system (Velmex, Bloomfield, NY, USA). The pre-amplified signal of the hydrophone is recorded by a digital oscilloscope (Tektronix, Beaverton, OR, USA). The wave generator, data acquisition and the positioning of the plate and hydrophone are computer controlled by a PC. The recording of the signal is triggered to start after a specific delay from the launch of the transducer signal. Several cycles of hydrophone signal are recorded and the time-domain data is Fourier transformed into the frequency-domain using a PC.

A detailed geometry of plate and measurement planes are shown in Fig. 2. The transducer is in the $y = 0$ plane and waves propagate in the direction of the positive y-axis. The front face of a plate is located at 45 mm distance from the transducer. The distance from the transducer to the center of the measurement planes is 85 mm. The plates are rotated in the (x,y)-plane. The measurement planes have the origin at the point (0, 85 ,0) mm. The (x,y)-plane is in $[-15, 15] \times [70, 100]$ mm. The measurements in this plane are used for comparison with the simulated fields.

Another 30 × 30 mm plane measurement is in the (x,z)-plane spanning over the region $[-15, 15] \times [-15, 15]$ mm. The data from this plane is used for the reconstruction of the transducer's surface velocity.

In this case the field is measured without the plastic plates. In both planes, the fields are scanned with 0.5 mm spacing.

[Figure 2 about here.]

V. SIMULATION PROCEDURE

The 3D Helmholtz-UWVF model used in this study is essentially the same as introduced in [24]. The computational region of interest has dimensions $40 \times 102 \times 40$ mm. All faces, except the transducer face $y = 0$, are surrounded by a 5 mm thick PML. In the PML, the decay of the field is obtained via a complex stretching of spatial variables [24], [56] so that spatial variables (x, y, z) are replaced by

$$\xi' = \begin{cases} \xi + \frac{i}{\kappa} \int_{\xi_0}^{\xi} \varsigma_0 (|\xi| - \xi_0)^n d\xi, & |\xi| \geq \xi_0, \\ \xi, & |\xi| < \xi_0, \end{cases} \tag{5}$$

where $\xi = x, y$ or z. Since the layer is 5 mm thick, the boundaries of the PML are $x_0 = 20$ mm, $y_0 = 102$ mm and $z_0 = 20$ mm. An efficient damping results in if the decay parameters are set to $n = 0$ and $\varsigma_0 = 400$ 1/m [24].

A cross-section of the simulation geometry is shown in Fig. 2. Since the plates pass through the computational domain, they continue at the same angle in the PML region. The PML decay parameter in the plate is same as in water $\sigma_0 = 400$ 1/m.

The transducer is modeled as an oscillating surface on which the normal derivative of the pressure is

$$\frac{\partial p}{\partial n} = i\omega\rho v_n. \tag{6}$$

However, unlike in a test problem of [24] where the normal velocity amplitude v_n was constant throughout the transducer surface, it can now be a function of location $v_n = v_n(x, z)$.

The planar circular transducer in Fig. 2 is located in the $y = 0$ plane and it is centered at the origin. Hence, the complex normal velocity v_n on the transducer surface S can be written in the form

$$v_n(x, z) = A(x, z)e^{-i\phi(x,z)},$$

where $A(x, y)$ is the amplitude and $\phi(x, z)$ is the phase.

The spatially varying amplitude and phase are computed as the solution of the inverse problem (4). The implementation of the velocity is carried out in two steps. First, the complex valued velocity is solved from (4) in a relatively dense set of point on the transducer surface. Second, the amplitude and phase of the velocity are represented in a parametrized form which simplifies the implementation of the velocity to the UWVF code.

The measurements of Section VI will show that the amplitude on the circular transducer used in this study, can be approximated with a radial Gaussian distribution

$$A = A_0 e^{-\frac{R^2}{2\sigma^2}}, \tag{7}$$

where A_0 is a real constant, $R = \sqrt{x^2 + z^2}$ and σ is the standard deviation. The phase is parametrized using a fifth order polynomial

$$\phi(x, z) = \sum_{\ell=0}^{5} \sum_{m=0}^{5-\ell} B_{\ell,m} x^{\ell} z^{m}. \tag{8}$$

Theoretical analysis of Gaussian sources in [57] showed that they have notably smoother near field behavior than ideal piston oscillators.

The standard deviation σ for the amplitude and the constants $B_{\ell,m}$ for the phase are obtained by a non-linear and linear (respectively) fitting to the reconstructed surface velocity data. If calibrated hydrophones are used to measure the pressure field for the inverse problem, the absolute value of the constant A_0 can also be computed from the reconstructed surface velocity field. Hence, absolute pressure values of simulated fields should correspond to experimental measurements (provided that the driving conditions of the transducer remain unchanged). However, since this study is limited to compare relative pressure amplitudes only, the amplitude parameter is set to $A_0 = 1$.

The UWVF code used in the simulations is coded with Fortran90 and parallelized using MPI (Message Passing Interface). The computations are done on a Beowulf PC cluster consisting of 24 2.6 GHz Pentium 4 processors and having 48 GB total RAM. The processors are networked using a 1 GB ethernet switch. Typically, computational meshes consisted of 40 000-80 000 tetrahedral elements and the number of plane basis function per an element varied between 1-90. Therefore, simulations of this study had about 2 millions degrees of freedom, required approximately 2 000 seconds of CPU time and 10 GB of memory.

Similarly as in [24], meshes were generated so that a typical maximum length of an element edge was about two wavelengths. In addition, using the method developed in [43], the number of basis functions for each element was chosen according to the condition number of the corresponding invertible matrix block, see [43] and [24] for details. The condition number of the blocks was limited below 10^5. The accuracy of the UWVF method for the 3D benchmark problems in [24] is below 1 % when slightly coarser meshes but a larger condition number (10^6) are used. Simulations of [43] show that the accuracy of the method can be increased either by refining the mesh or by allowing a higher condition number (which in turn results in a higher dimensional basis).

VI. COMPARISON BETWEEN MEASUREMENTS AND SIMULATIONS

The experimentally measured pressure field in the plane $y = 85$ mm without a plate is shown in Fig. 3. This field is used as input data to the inverse problem (4) for reconstructing the surface velocity distribution of the transducer. For the discrete Rayleigh integral (3), the transducer surface is divided into 2378 elements on which the discrete velocity is sought. On the other hand, the field in the plane $y = 85$ mm is measured in a 30 × 30 mm region with 0.5 mm spacing which corresponds to 3721 measurement points.

[Figure 3 about here.]

The Tikhonov regularized solution of the over-determined matrix system is computed using $\gamma = 2.2 \cdot 10^5$ as the regularization parameter. The parameter is chosen by trial-and-error. Namely, at low values of γ, the solution is unstable until the increase in γ over a certain value stabilizes the solution. Further increase in the regularization parameter tends to force the solution toward a constant value of $v_{n,j} = 0$ for all $j = 1, ..., N$ since this minimizes the side constraint $\gamma||v_n||^2$ [52]. Although methods for choosing the regularization parameter has been developed (e.g. L-curve and generalized cross-validation (GCV) methods used in [53]), the exact solution for γ is not available. In this study, several simulations showed that the parameter value $\gamma = 2.2 \cdot 10^5$ gives a suitable balance between the constant and unstable solution for the velocity distribution v_n.

The convergence of the inverse problem as a function of the regularization parameter γ and the density of the surface discretization λ/h are shown in Fig. 4. The parameter λ/h is the ratio of the wavelength and the maximum edge length of a triangle on the triangulated transducer surface. The norm $||\partial v_n||$ shows the relative difference of the velocity distribution v_n between two adjacent values of γ or λ/h.

The graph on the left shows that the relative residual $||p - Hv_n||$ remains small at low values of γ. In the region $\gamma > 2 \cdot 10^5$ the residual starts to increase while the norm of the velocity distribution $||v_n||$ reduces due to the increasing effect of the Tikhonov regularization term $\gamma^2||v_n||$. On the other hand, there is a range of values of γ where the change in v_n (i.e. the norm $||\partial v_n||$) is small. The chosen value $\gamma = 2.2 \cdot 10^5$ is on the upper end of this range. At the low values of the regularization parameter the norm $||\partial v_n||$ is large due to the instability of the inverse problem and at a large value of γ, the norm increases due to the effect of the term $\gamma^2||v_n||$.

The figure of the right indicates that the solution of the inverse problem stabilizes when $\lambda/h > 2$. The following inverse problem of this study is solved using $\lambda/h = 2.5$.

[Figure 4 about here.]

The normalized solution for the velocity distribution is shown in Fig. 5. The amplitude and phase are shown a dense set of points on the transducer plane. In order to use spatially varying velocity in the UWVF, the amplitude and phase are parametrized.

[Figure 5 about here.]

Results indicate that the amplitude has almost a radially Gaussian shape which justifies the Gaussian parametrization (7) for the UWVF method. More precisely, the non-linear fitting gives a value $\sigma = 7.4$ mm for the standard deviation. The behavior of the phase is more complicated and therefore the high-order polynomial representation (8) was chosen. Even higher order polynomials could be used but in this case, the least-squares fit to the phase data became unstable if the order was increased. The parametrized amplitude and phase are shown in the Fig. 5.

The amplitude of UWVF approximation of the pressure field on the central axis of the transducer is presented in Fig. 6. The field is computed using the parametrized surface velocity that is resolved from the measurements in the plane $y = 85$ mm and normalized using the value at the point (0,85,0) mm. In comparison to the ideal piston model, the near-field behavior of the field is smoother due to the Gaussian velocity distribution.

[Figure 6 about here.]

The simulated and measured fields without a plate are compared in the $y = 85$ mm plane in the Fig. 3 and more detailed in the (x, y)-plane in Fig. 7. To simplify the comparison between the amplitudes of the simulated and measured fields, all fields from here on are normalized with the amplitude at the point (0,85,0) mm in the absence of a plate. More precisely, simulated fields are normalized using the simulated value at (0,85,0) mm and measured fields are normalized using the corresponding experimental value.

[Figure 7 about here.]

The accuracy of the amplitude $|p|$ and phase of simulations are investigated separately. The error in the amplitude is computed as a discrete L^2-error in the form

$$\epsilon_{|p|} = 100\sqrt{\frac{\sum_{m=1}^{M}(|\hat{p}_m| - |p_m|)^2}{\sum_{m=1}^{M}|\hat{p}_m|^2}}, \tag{9}$$

where $\hat{p}_m$ and p_m are the measured and simulated fields in the mth point. The phase error is measured as a mean difference between measured and simulated phases

$$\epsilon_{\arg p} = \frac{1}{M} \sum_{m=1}^{M} |\arg \hat{p}_m - \arg p_m|. \tag{10}$$

The 360° periodicity is taken into account in the phase error. Therefore the absolute phase difference never exceeds 180°.

The errors of the amplitude and phase in the absence of a plate (Fig. 7) are 3.4 % and $6.6^\circ \pm 11.1^\circ$, respectively. The uncertainty range of the phase is shown as one standard deviation (SD).

The effect of the plastic plate on the transmitted field is analyzed next. In Fig. 8 the UWVF solution inside the non-PML region is shown for Plate 1 and Plate 2. The fields are presented for the different rotation angles of the plate.

[Figure 8 about here.]

Simulated and measured pressure amplitudes in the 30×30 mm plane behind the plate are compared in Fig. 9. The amplitudes are normalized with the value of pressure at the point (0,85,0) mm (i.e. at the center of the measurement plane) in the absence of a plate. Pressure amplitudes and phase along line $y = 85$ mm and $x = 0$ mm for Plate 1 are presented in Fig. 10. Corresponding results for Plate 2 are shown in Fig. 11. Phase and amplitude errors as a function of incident angle for both plates are listed in Table II.

[Table 2 about here.]

[Figure 9 about here.]

[Figure 10 about here.]

[Figure 11 about here.]

In the case of Plate 1 with $\theta = 0$ deg., the amplitude of the simulated field is over-estimated. On the other hand, for Plate 2 with $\theta = 0$ deg., there is a relatively large discrepancy in phases.

For both plates, the best agreement between simulations and measurements is obtained when the plate is rotated in $\theta = 10$ deg. The agreement for the Plate 1 is excellent while a shift in the radial amplitude profile can be observed for Plate 2.

Although, the amplitudes start to deviate in $\theta = 20$ deg., phases are still in rather good agreement. The amplitude for Plate 1 and $\theta = 20$ deg. shows a relative large radial shift in the beam profile at line $y = 85$

mm and therefore there is disagreement in the axial amplitude in the axis $x = 0$ mm. In the case of Plate 2, the amplitude of the simulated field is over-estimated.

For the largest angle $\theta = 30$ deg., the error either in the amplitude or in the phase is notable. The amplitude profiles for Plate 1 are still in rather good agreement but the phase has an extensive error. Both phase and amplitude are erroneous for Plate 2.

VII. DISCUSSION AND CONCLUSIONS

In this study, the feasibility of the UWVF model for the Helmholtz equation was investigated for simulating continuous-wave ultrasound fields in inhomogeneous media. The computational simulations were compared with experimental measurements in the case of ultrasound propagation through plastic plates. Two plates were used. Plate 1 was of a single layer of plastic 1. Plate 2 consisted of a layer of rubber sandwiched between layers of plastic 2. The sound field was generated using a planar circular PZT transducer operating at 531 kHz. Transmitted fields behind the plates were measured for different incident angles of the sound beam.

The velocity distribution on the transducer was reconstructed as a solution of the Tikhonov regularized inverse problem. The parametrized form of the velocity was used in computing the source term for the UWVF model.

A reasonable agreement was found between the measurements and the Helmholtz model for both plates on low incident angles. However, on larger angles, the accuracy of the simulations deteriorated. For both plates, the simulations become unreliable when the angle of the plate was larger than 20 degrees.

There are several possible candidates for the cause of inaccuracy of the simulations. For example, the Helmholtz model does not take into account the generation other than longitudinal waves. In the plastic plates, however, the mode conversion into other types of elastic waves is possible, especially on large incident angles. This is the most probable cause to the failure of the Helmholtz model for the largest incident angle $\theta = 30$ deg. The use of a coupled fluid-elastic partial wave model has been shown to improve the accuracy compared to a model that omits the generation of shear waves [58].

Another drawback in the simulations of this study was that the transducer was modeled as a perfectly rigid surface for back scattered waves. In practice, the performance of the PZT transducer may be altered by the standing waves between the plates and the transducer [59]. Particularly, back-scattered waves from the plate hit the transducer and may therefore disturb the generation of the sound from the PZT element. Back-scattered waves are a possible reason for the discrepancies between simulations and measurements at small angles of the plates such as was observed for both plates with $\theta = 0$. The modeling of the transducer can be improved by using piezo-electric equations for the PZT element. This kind of approach for transducer modeling has been utilized in [60], [61]. However, those modeling studies did not consider the effect of back-scattered waves on the output of the transducer.

Despite the limitations observed at large incident and relatively large computational requirements, the 3D full-wave Helmholtz model may be feasible for large-scale ultrasound simulations. Particularly, if mode conversion has a negligible effect on the sound field since one can expect that the Helmholtz model better approximates CW sound propagation in inhomogeneous fluid media (opposed to solid plastic plates investigated in this study where other than dilatational waves may be generated). An application in authors' interest for the UWVF method is the modeling of transcranial transmission of CW ultrasound fields. Therefore, the feasibility of the Helmholtz UWVF model for transmission through solid layers was investigated. The results suggest that the Helmholtz model alone is not sufficient to approximate the chosen transmission problem accurately. However, the mode conversion in the plates can be taken into account by coupling UWVF methods for the fluid (Helmholtz model) and for the elastic structure (Navier model, see [44]). The coupled fluid-structure method is currently developed and is a topic of a future study.

On the other hand, it is unlikely that the error in the model at low incident angles is due to the mode conversion. While the disturbance in the transducer output due to standing waves may be a possible cause of the disagreement a more detailed investigation is needed to analyze the source of this error.

ACKNOWLEDGMENT

This study has been supported by the Finnish Academy Grants 44042,54065,72431,77818,80773 and 200627, by the Finnish Cultural Foundation of Northern Savo, by Jenny and Antti Wihuri Foundation, by the Foundation for Advanced Technology of Eastern Finland and NIH Grant CA076550.

REFERENCES

[1] E. Béchet, J.-C. Cuilliere, and F. Trochu, "Generation of a finite element MESH from stereolithography (STL) files," *Computer-Aided Design*, vol. 34, no. 1, pp. 1–17, 2002.

[2] Y. Botros, J. Volakis, P. VanBaren, and E. Ebbini, "A hybrid computational model for ultrasound phased-array heating in the presence of strongly scattering obstacles," *IEEE Transactions on Biomedical Engineering*, vol. 44, no. 11, pp. 1039–1050, 1997.

[3] E. Kühnicke, "Three-dimensional waves in layered media with nonparallel and curved interfaces: A theoretical approach," *The Journal of the Acoustical Society of America*, vol. 100, no. 2, pp. 709–716, 1996.

[4] Y. Botros, E. Ebbini, and J. Volakis, "Two-step hybrid virtual array-ray (VAR) technique for focusing through the rib cage," *IEEE Transactions on Ultrasonics, Ferroelectrics, and Frequency Control*, vol. 45, no. 4, pp. 989–1000, 1998.

[5] X. Fan and K. Hynynen, “The effect of wave reflection and refraction at soft tissue interfaces during ultrasound hyperthermia treatments,” *The Journal of the Acoustical Society of America*, vol. 91, no. 3, pp. 1727–1736, 1992.

[6] P. Stepanishen and K. Benjanim, “Forward and backward projection of acoustic fields using FFT methods,” *The Journal of the Acoustical Society of America*, vol. 71, no. 4, pp. 803–812, 1982.

[7] M. Schafer, P. Lewin, and J. Reid, “Propagation through inhomogeneous media using the angular spectrum method,” in *Proceedings of IEEEUltrasonics Symposium*, 1987, pp. 943–946.

[8] C. Vecchio, M. Schafer, and P. Lewin, “Prediction of ultrasound field propagation through layered media using the extended angular spectrum method,” *Ultrasound in Medicine and Biology*, vol. 20, no. 7, pp. 611–622, 1994.

[9] G. Clement and K. Hynynen, “Field characterization of therapeutic ultrasound phased arrays through forward and backward planar projection,” *The Journal of the Acoustical Society of America*, vol. 108, no. 1, 2000.

[10] ——, “A non-invasive method for focusing ultrasound through the human skull,” *Physics in Medicine and Biology*, vol. 47, no. 8, pp. 1219–1236, 2002.

[11] G.T.Clement and K. Hynynen, “Forward planar projection through layered media,” *IEEE Transactions on Ultrasonics, Ferroelectrics, and Frequency Control*, vol. 50, no. 12, pp. 1689–1698, 2003.

[12] R. Schechter, K. Simmonds, N. Batra, R. Mignogna, and R. Delsanto, “Use of a transient wave propagation code for 3D simulation of cw radiated transducer fields,” *Ultrasonics*, vol. 37, pp. 89–96, 1999.

[13] N. Bojarski, “The k-space formulation of the scattering problem in the time domain,” *The Journal of the Acoustical Society of America*, vol. 72, no. 2, pp. 570–584, 1982.

[14] T. Mast, L. Souriau, D. Liu, M. Tabei, A. Nachman, and R. Waag, “A k-space method for large-scale models of wave propagation in tissue,” *IEEE Transactions on Ultrasonics, Ferroelectrics, and Frequency Control*, vol. 48, no. 2, pp. 341–354, 2001.

[15] B. Fornberg, *A Practical Guide to Pseudospectral Methods*. Cambridge University Press, 1995.

[16] H.-W. Chen, “Staggered-grid pseudospectral viscoacoustic wave field simulation in two-dimensional media,” *The Journal of the Acoustical Society of America*, vol. 100, no. 1, pp. 120–131, 1996.

[17] G. Wojcik, B. Fornberg, R. Waag, L. Carcione, J. Mould, L. Nikodym, and T. Driscoll, “Pseudospectral methods for large-scale bioacoustic models,” *IEEE Ultrasonics Symposium Proceeding*, vol. 2, pp. 1501–1506, 1997.

[18] D. Komatitsch, J.-P. Vilotte, R. Vai, J. M. Castillo-Covarrubias, and F. Sánchez-Sesma, “The spectral element method for elastic wave equations - application to 2-D and 3-D seismic problems,” *International Journal for Numerical Methods in Engineering*, vol. 45, no. 9, pp. 1139–1164, 1999.

[19] B. Després, “Sur une formulation variationnelle de type ultra-faible,” *Comptes Rendus de l’Academie des Sciences - Series I*, vol. 318, pp. 939–944, 1994.

[20] O. Cessenat, “Application d’une nouvelle formulation variationelle des equations d’ondes harmonigues, problemes de Helmholtz 2D et de Maxwell 3D,” Ph.D. dissertation, Paris IX Dauphine, 1996.

[21] O. Cessenat and B. Després, “Application of an ultra weak variational formulation of elliptic PDEs to the two-dimensional Helmholtz problem,” *SIAM Journal of Numerical Analysis*, vol. 35, no. 1, pp. 255–299, 1998.

[22] ——, “Using plane waves as base functions for solving time harmonic equations with the ultra weak variational formulation,” *Journal of Computational Acoustics*, vol. 11, no. 2, pp. 227–238, 2003.

[23] J. Bérenger, “A perfectly matched layer for the absorption of electromagnetic waves,” *Journal of Computational Physics*, vol. 114, pp. 185–200, 1994.

[24] T. Huttunen, J. Kaipio, and P. Monk, “The perfectly matched layer for the ultra weak variational formulation of the 3D Helmholtz problem,” *International Journal for Numerical Methods in Engineering*, 2004, in Press.

[25] A. Pierce, *Acoustics: An Introdunction to Its Physical Principles and Applications*. The Acoustical Society of America, 1981.

[26] I. Harari and E. Turkel, “Accurate finite difference methods for time-harmonic wave propagation,” *Journal of Computational Physics*, vol. 119, no. 252-270, 1995.

[27] F. Ihlenburg, *Finite Element Analysis of Acoustic Scattering*. New York: Springer, 1998.

[28] P. Kythe, *An Introdunction to Boundary Element Methods*. CRC PRess, 1995.

[29] K. Gerdes and F. Ihlenburg, “On the pollution effect in FE solutions of the 3D-Helmholtz equation,” *Computer Methods in Applied Mechanics and Engineering*, vol. 170, pp. 155–172, 1999.

[30] A. Oberai and P. Pinsky, “A numerical comparison of finite element methods for the Helmholtz equation,” *Journal of the Computational Acoustics*, vol. 8, no. 1, pp. 211–221, 2000.

[31] D. Colton and R. Kress, *Inverse Acoustic and Electromagnetic Scattering Theory*. Springer-Verlag, 1992.

[32] R. Kress, *Linear Integral Equations*. Springer-Verlag, 1989.

[33] D. Burnett, “A three-dimensional acoustic infinite element based on a prolate spheroidal multipole expansion,” *The Journal of the Acoustical Society of America*, vol. 96, no. 5, pp. 2798–2816, 1994.

[34] I. Harari and T. Hughes, “A cost comparison of boundary element and finite element methods for problems of time-harmonic acoustics,” *Computer Methods in Applied Mechanics and Engineering*, vol. 97, pp. 77–102, 1992.

[35] R. Coifman, V. Rokhlin, and S. Wandzura, “The fast multiple method for the wave equation: a pedestrian prescription,” *IEEE Antennas and Propagation Magazine*, vol. 35, no. 3, pp. 7–12, 1993.

[36] E. Darve, “The fast multipole method: numerical implementation,” *Journal of Computational Physics*, vol. 160, pp. 195–240, 2000.

[37] V. Rokhlin, “Rapid solution of integral equations of scattering theory in two dimensions,” *Journal of Computational Physics*, vol. 86, no. 2, pp. 414–439, 1990.

[38] I. Babuška and J. Melenk, “The partition of unity method,” *International Journal for Numerical Methods in Engineering*, vol. 40, pp. 727–758, 1997.

[39] O. Laghrouche, P. Bettess, and R. Astley, “Modelling of short wave diffraction problems using approximating systems of plane waves,” *International Journal for Numerical Methods in Engineering*, vol. 54, pp. 1501–1533, 2002.

[40] P. Monk and D. Wang, “A least squares method for the Helmholtz equation,” *Computer Methods in Applied Mechanics and Engineering*, vol. 175, pp. 121–136, 1999.

[41] C. Farhat, I. Harari, and L. Franca, “The discontinuous enrichment method,” *Computer Methods in Applied Mechanics and Engineering*, vol. 190, pp. 6455–6479, 2001.

[42] C. Farhat, I. Harari, and U. Hetmaniuk, “A discontinuous Galerkin method with Lagrange multipliers for the solution of Helmholtz problems in the mid-frequency regime,” *Computer Methods in Applied Mechanics and Engineering*, vol. 192, pp. 1389–1419, 2003.

[43] T. Huttunen, P. Monk, and J. Kaipio, “Computational aspects of the ultra-weak variational formulation,” *Journal of Computational Physics*, vol. 182, pp. 27–46, 2002.

[44] T. Huttunen, P. Monk, F. Collino, and J. Kaipio, “The ultra weak variational formulation for elastic wave problems,” *SIAM Journal on Scientific Computing*, vol. 25, no. 5, pp. 1717 – 1742, 2004.

[45] D. Givoli, “Non-reflecting boundary conditions,” *Journal of Computational Physics*, vol. 94, pp. 1–29, 1991.

[46] T. Huttunen, J. Kaipio, and K. Hynynen, “Modeling of anomalies due to hydrophones in continuous-wave ultrasound fields,” *IEEE Transactions on Ultrasonics, Ferroelectrics, and Frequency Control*, vol. 50, no. 11, pp. 1486–1500, 2003.

[47] D. Hutchins, H. Mair, P. Puhach, and A. Osei, “Continuous-wave pressure fields of ultrasonic transducer,” *The Journal of the Acoustical Society of America*, vol. 80, no. 1, pp. 1–12, 1986.

[48] M. Schafer and P. Lewin, “Transducer characterization using the angular spectrum method,” *The Journal of the Acoustical Society of America*, vol. 85, no. 5, pp. 2202–2214, 1989.

[49] X. Fan, E. Moros, and W. Straube, "Acoustic field prediction for a single planar continuous-wave source using an equivalent phased array method," *The Journal of the Acoustical Society of America*, vol. 102, no. 5, pp. 2734–2741, 1997.

[50] E. Ebbini and C. Cain, "Multiple-focus ultrasound phased-array pattern synthesis: optimal driving-signal distributions for hyperthermia," *IEEE Transactions on Ultrasonics, Ferroelectrics, and Frequency Control*, vol. 36, no. 5, pp. 540–548, 1989.

[51] ——, "A spherical-section ultrasound phased array applicator for deep localized hyperthermia," *IEEE Transactions on Biomedical Engineering*, vol. 38, no. 7, pp. 634–643, 1991.

[52] P. Hansen, *Rank-Deficient and Discrete Ill-Posed Problems: Numerical Asptects of Linear Inversion*. SIAM, 1998.

[53] A. Schuhmacher, J. Hald, K. Rasmussen, and P. Hansen, "Sound source reconstruction using inverse boundary element calculations," *The Journal of the Acoustical Society of America*, vol. 113, no. 1, pp. 114–127, 2003.

[54] A. Tihonov, "Regularization of incorrectly posed problems," *Soviet Mathematics - Doklady*, vol. 4, pp. 1624–1627, 1963.

[55] B.-N. Hung and A. Goldstein, "Acoustic parameters of commercial plastics," *IEEE Transactions on Sonics and Ultrasonics*, vol. SU-30, no. 4, pp. 249–254, 1983.

[56] W. Chew and W. Weedon, "A 3D perfectly matched medium from modified Maxwell's equations with stretched coordinates," *Microwave and Optical Technology Letters*, vol. 7, no. 13, pp. 599–604, 1994.

[57] M. Greenspan, "Piston radiator: some extensions of the theory," *The Journal of the Acoustical Society of America*, vol. 65, no. 3, pp. 608–621, 1979.

[58] G. T. Clement, P. J. White, and K. Hynynen, "Enhanced ultrasound transmission through the human skull using shear mode conversion," *The Journal of the Acoustical Society of America*, vol. 115, no. 3, pp. 1356–1364, 2004.

[59] K. Beissner, "The influence of membrane reflections on ultrasonic power measurements," *Acustica*, vol. 50, pp. 194–200, 1982.

[60] N. Abboud, G. Wojcik, D. Vaughan, J. Mould, D. Powell, and L. Nikodym, "Finite element modeling for ultrasonics transducers," in *Proceedings of SPIE's International Symposium, Medical Imaging*, vol. 3341, San Diego, Feb. 21-27 1998.

[61] R. Schechter, K. Simmonds, and R. Mignogna, "Computational and experimental investigation of the fields generated by a 1-3 piezocomposite transducer," *Ultrasonics*, vol. 39, no. 3, pp. 153–234, 2001.

LIST OF FIGURES

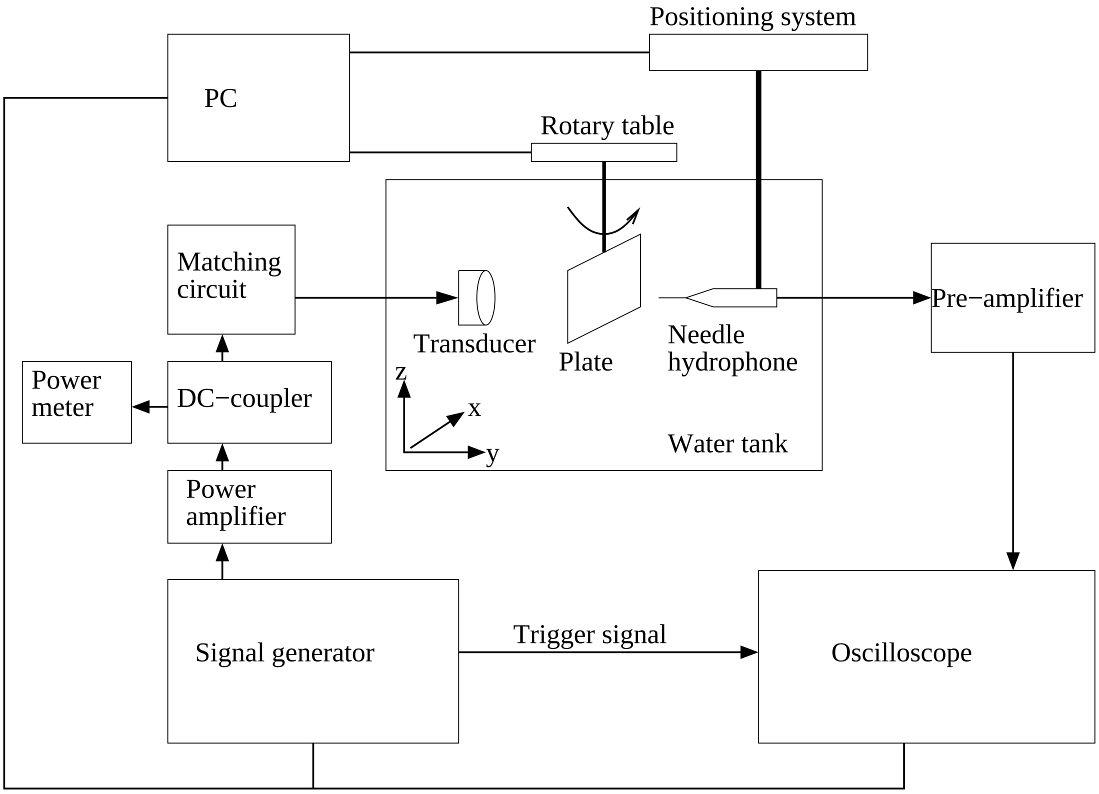

Fig. 1. A block diagram of the experimental setup.

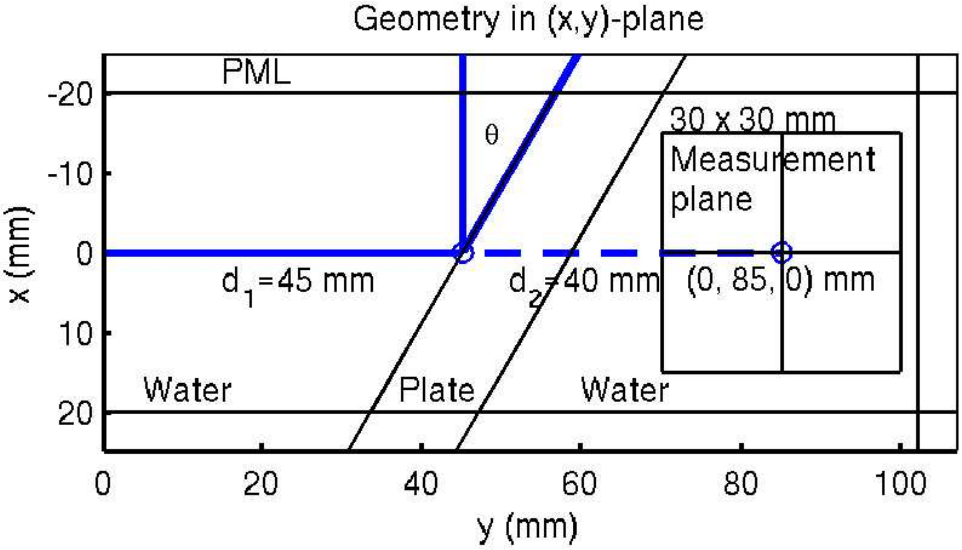

Fig. 2. Rotation of the plate and measurement geometry. The field is emitted by a planar circular transducer with the diameter 30 mm. The transducer is located in the $y = 0$ plane so that the center of the transducer is at the origin. The front face of the plate is located 40 mm from the transducer and the center of measurement planes is 85 mm from the transducer. The square region shows the (x, y)-measurement plane. The rotation angle of the plate is denoted by θ.

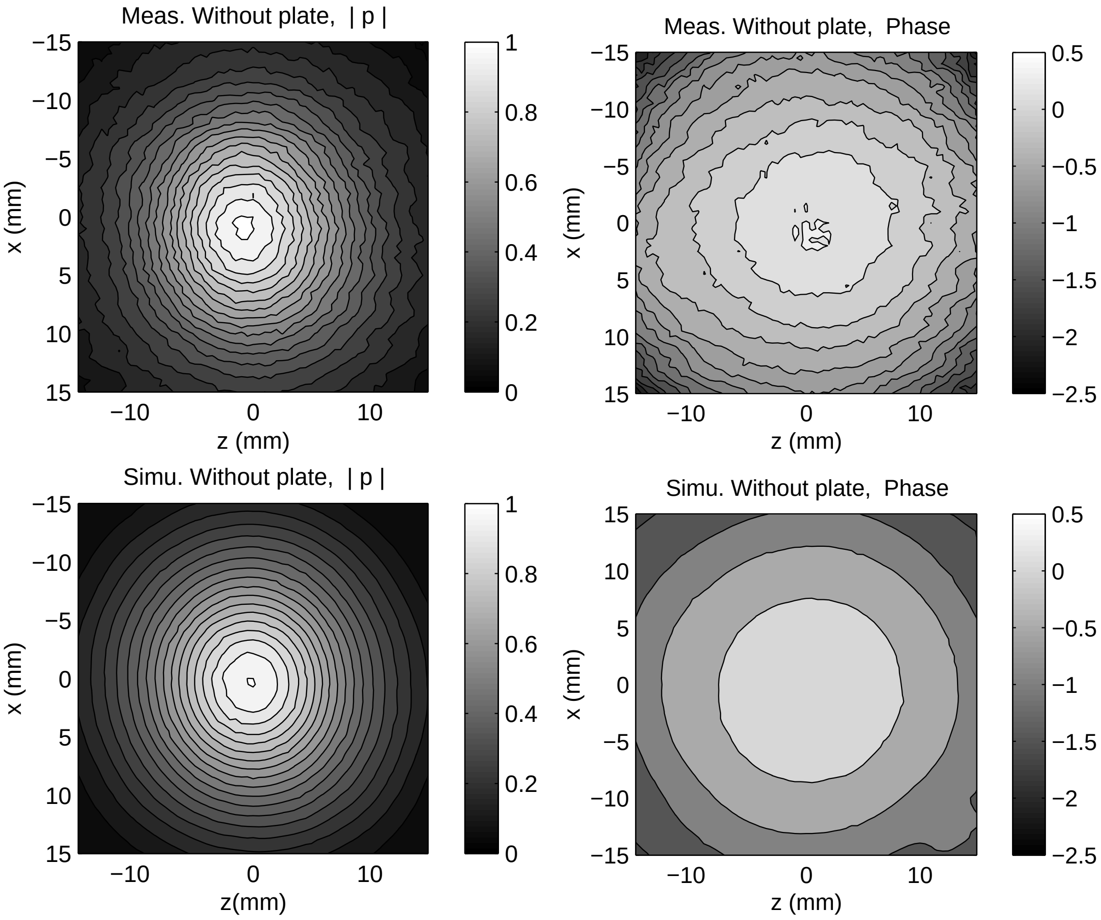

Fig. 3. The measured field without a plate in the plane $y = 85$ mm (top row). The simulated field in the same plane using the reconstructed surface velocity distribution of Fig. 5 (bottom row). The amplitudes are normalized using the value of —p— at the point (0, 85, 0) mm.

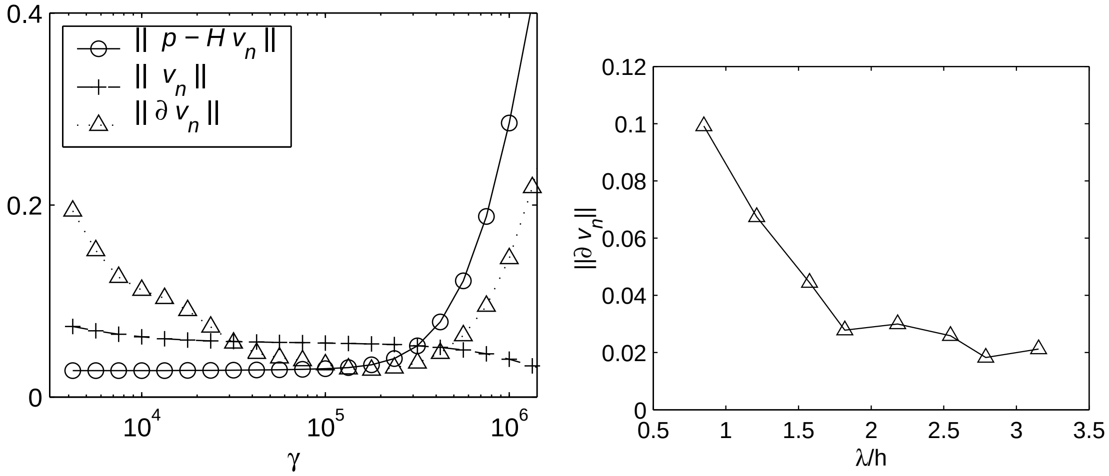

Fig. 4. A discrete L^2-norm of $p - Hv_n$, v_n and ∂v_n as a function of the regularization parameter γ (Left). The norm of ∂v_n as the function of the density of the surface partition λ/h for $\gamma = 2.2 \cdot 10^5$ is shown on the right. The norm $||\partial v_n||$ shows the relative difference of the velocity distribution v_n between two adjacent values of γ or λ/h.

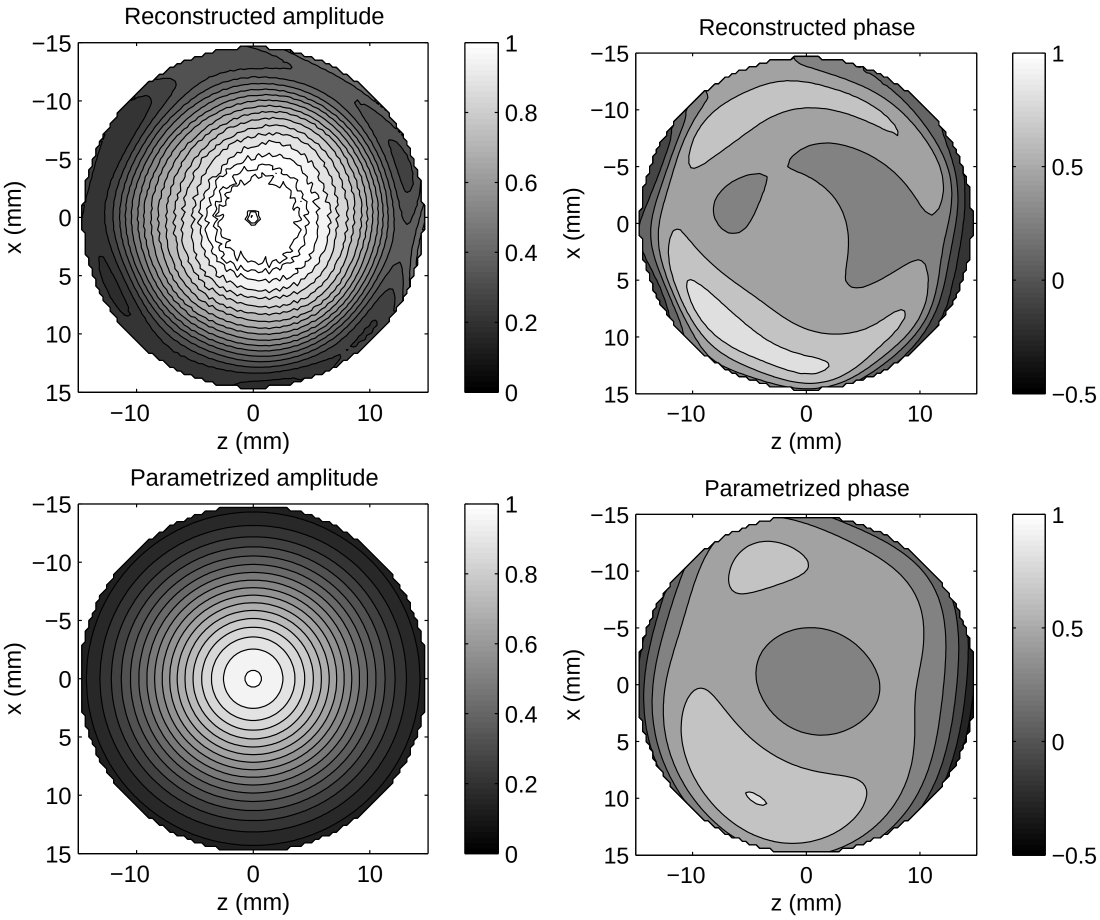

Fig. 5. Amplitude (top left) and phase (top right) of the complex valued normal velocity amplitude on the transducer. The velocity is obtained as the solution of the inverse problem (4). Corresponding parametrized forms of the velocity amplitude are shown on the bottom row. These velocity profiles are used as a source in the UWVF simulations.

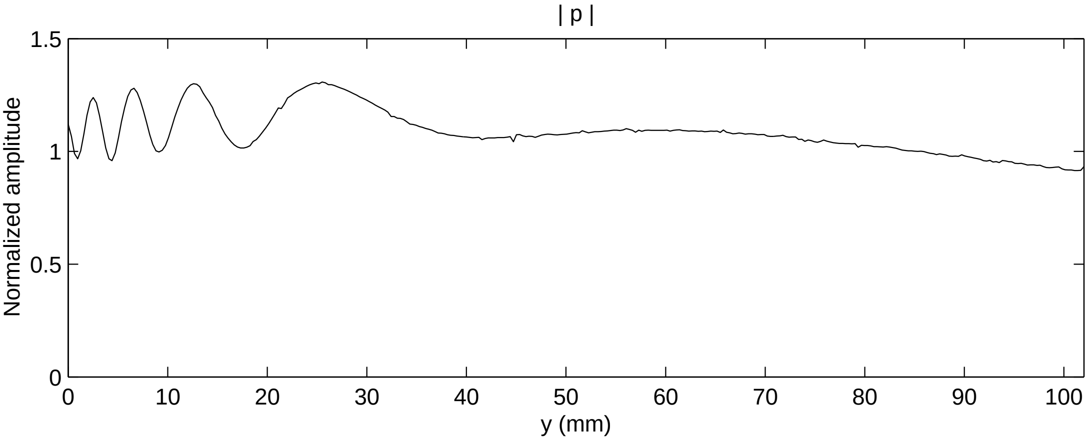

Fig. 6. The simulated amplitude on the central axis of the transducer in water using the parametrized form of the velocity profile of Fig. 5.

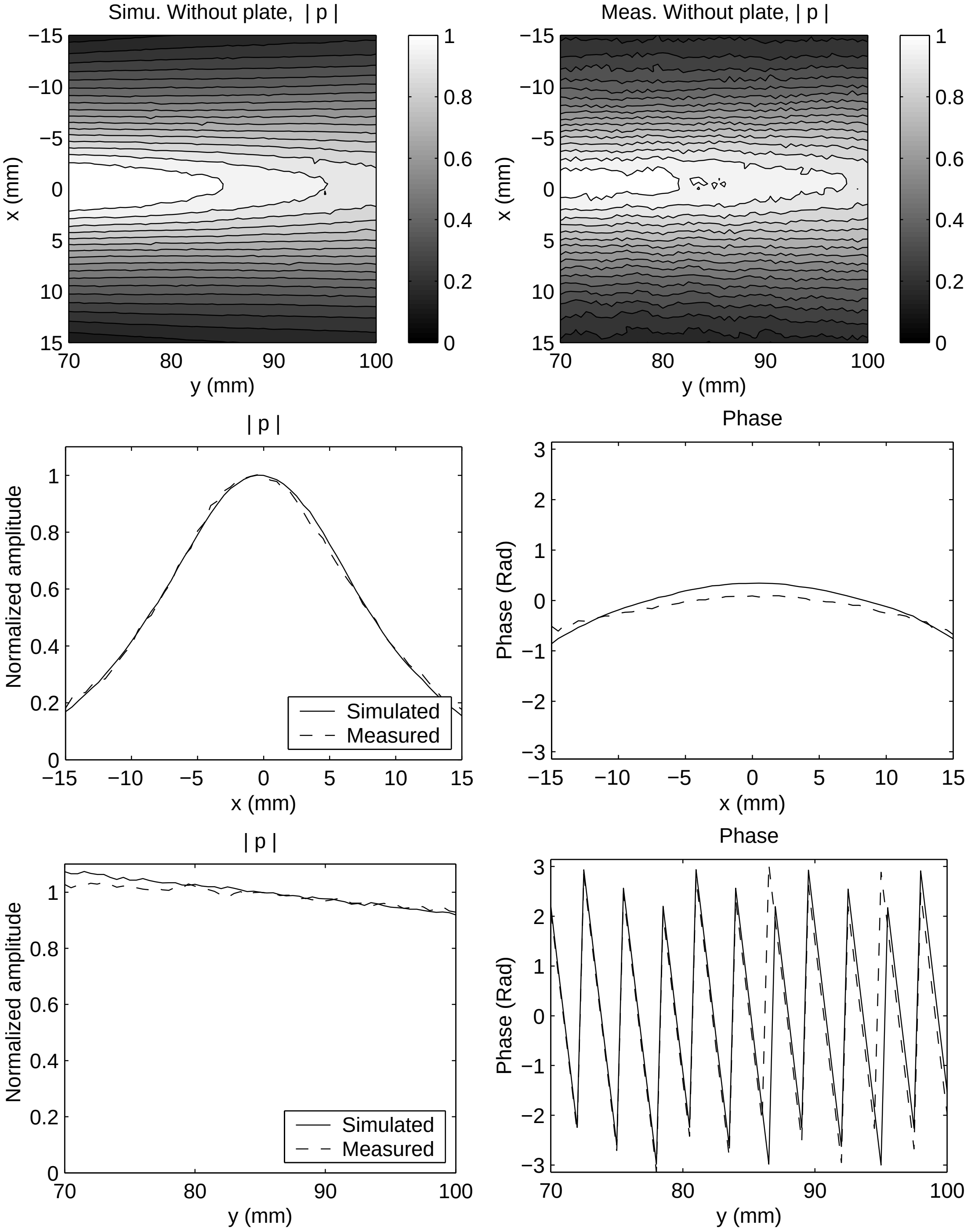

Fig. 7. Comparison of the measured and simulated fields in the absence of a plate. The fields are shown in whole the (x, y)-plane (top row) and; along the lines $y = 85$ mm (middle row) and $x = 0$ mm (bottom row).

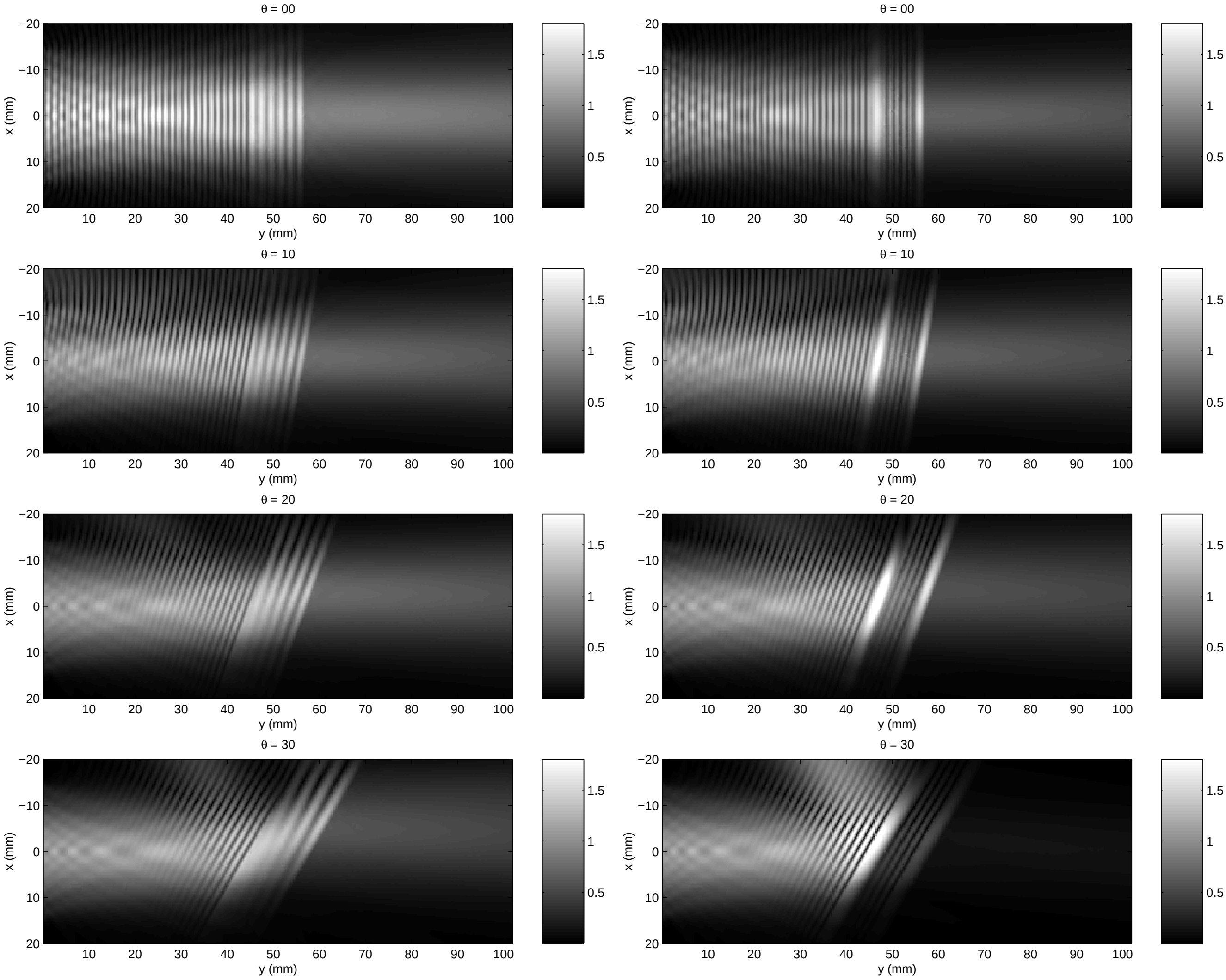

Fig. 8. Simulated pressure amplitudes $|p|$ in the non-PML region in the (x, y)-plane for the different angles of the plate. Fields for the single layer plate are shown in the first column and fields for the three layer plate are in the second column.

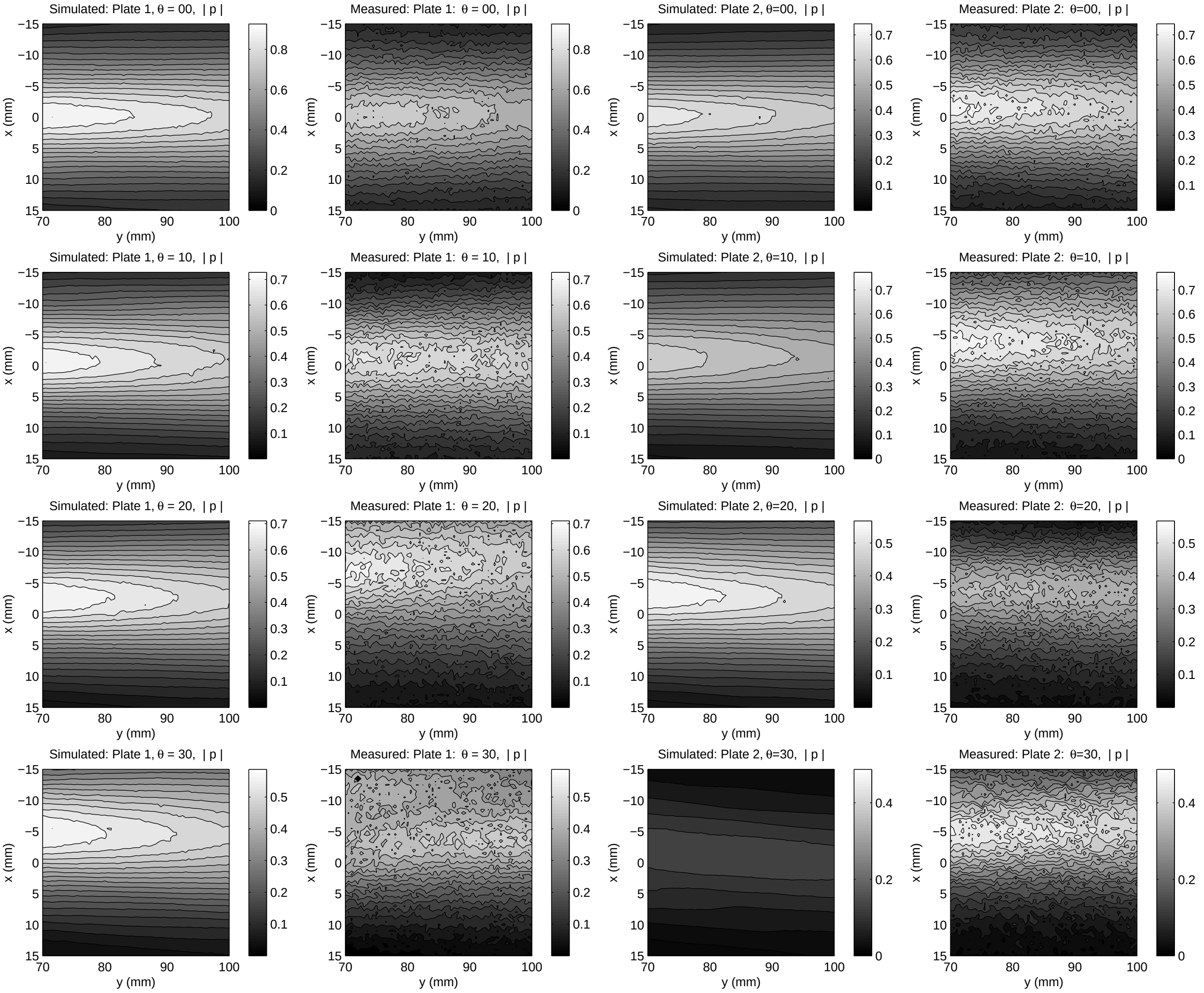

Fig. 9. Comparison of the measured and simulated pressure amplitudes at the 30×30 mm measurement plane behind a plate, see Fig. 2. The fields are normalized with the pressure value at the point (0,85,0) mm in the absence of a plate. First column: Simulated fields for Plate 1 and for incident angles $\theta = 0, 10, 20, 30$ deg (from top to bottom). Second column: Corresponding experimentally measured fields for Plate 1. Third column: Simulated fields for Plate 2 and for incident angles $\theta = 0, 10, 20, 30$ deg. Fourth column: Corresponding experimentally measured fields for Plate 2.

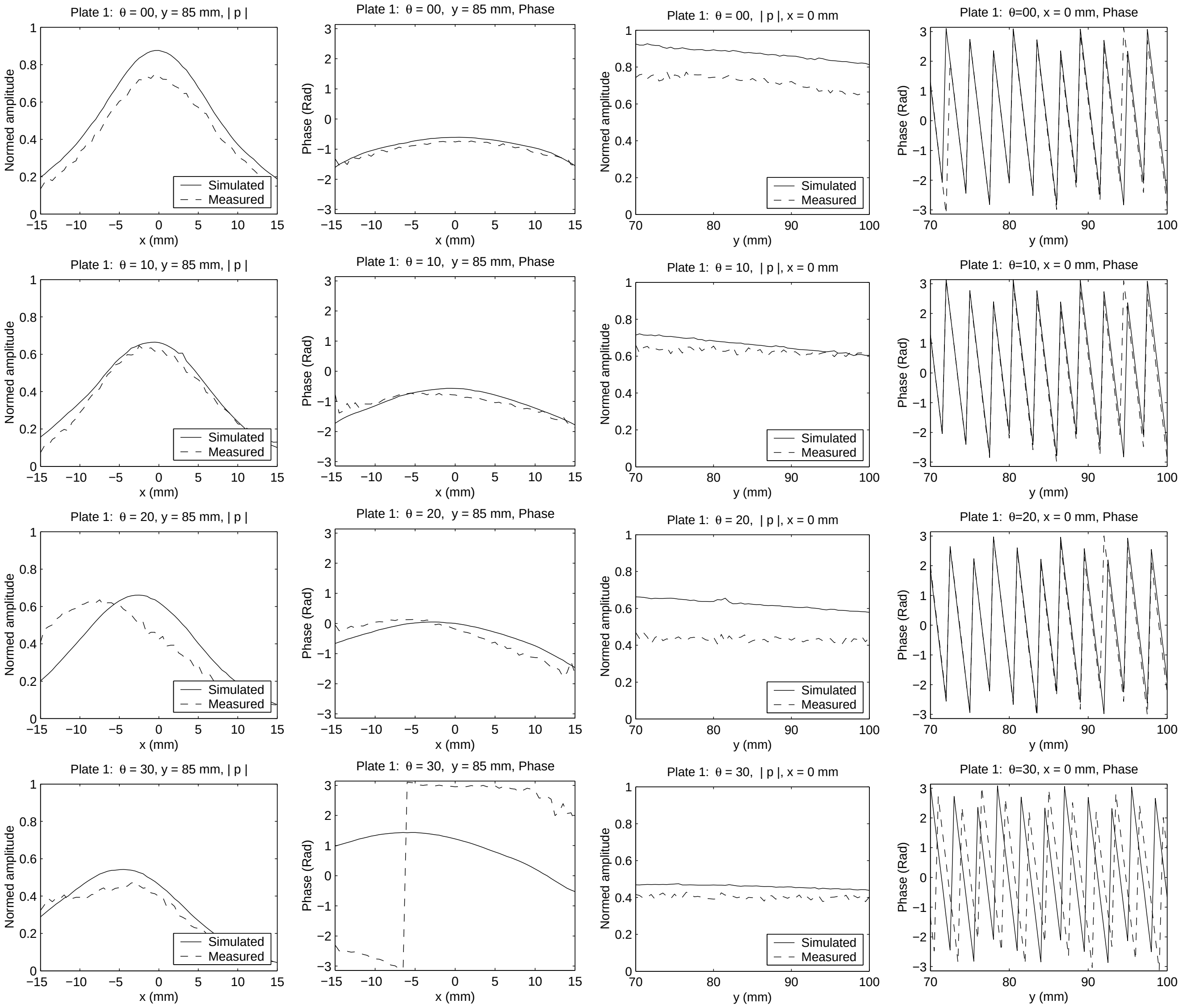

Fig. 10. Comparison of the measured and simulated pressure fields for the single layer plate (Plate 1). The amplitudes and phases are plotted along the axes $y = 85$ mm and $x = 0$ mm in the measurement plane, see Fig. 2. The amplitudes are normalized with the pressure value at the point (0,85,0) mm in the absence of a plate. First column: Pressure amplitudes on $y = 85$ mm axis for different incident angles. Second column: Phases of $y = 85$ mm axis. Third column: Pressure amplitudes on $x = 0$ mm axis for different incident angles. Fourth column: Phases of $x = 0$ mm axis.

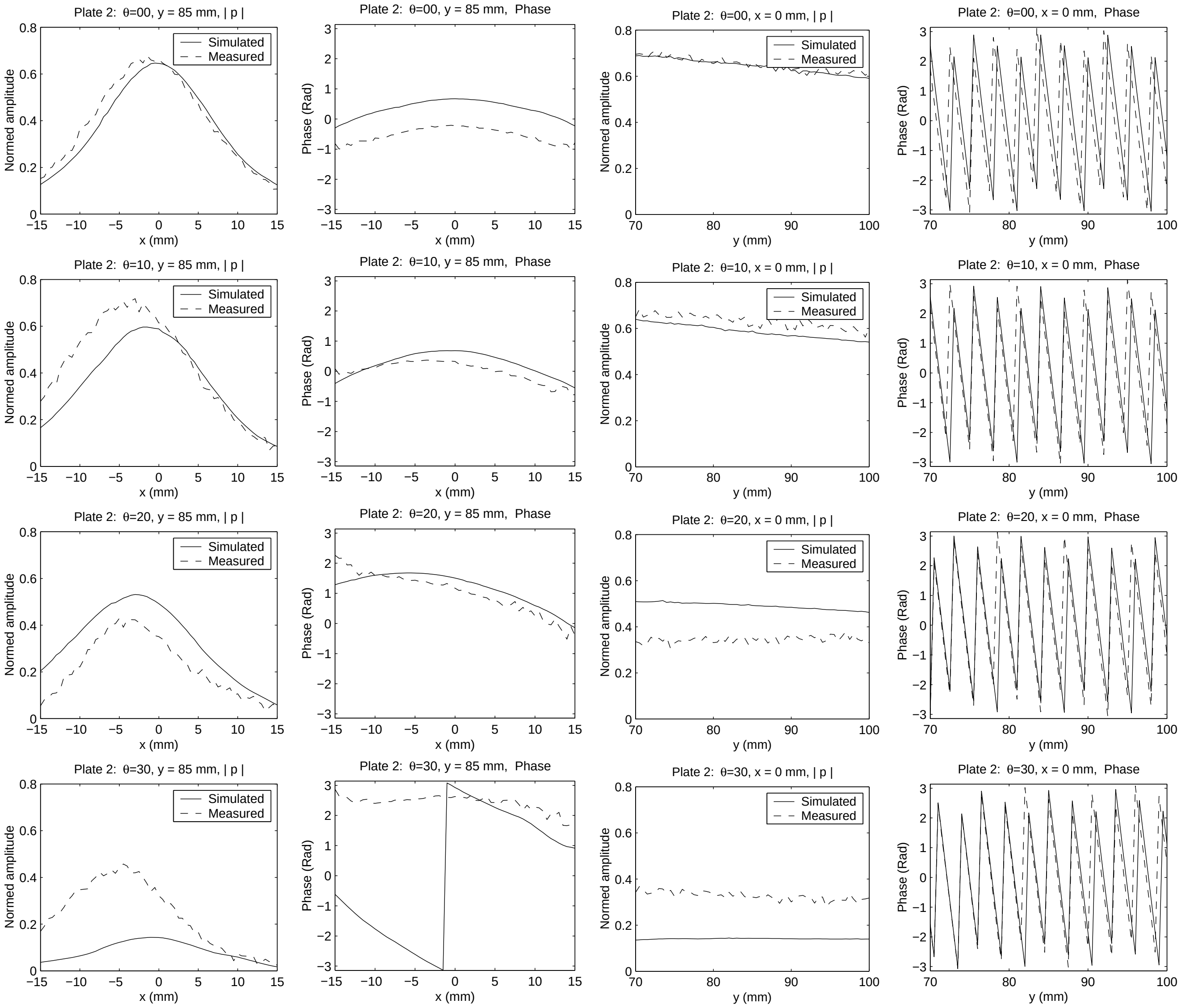

Fig. 11. Comparison of the measured and simulated pressure fields for the three layer plate (Plate 2). The amplitudes and phases are plotted along the axes $y = 85$ mm and $x = 0$ mm in the measurement plane, see Fig. 2. The amplitudes are normalized with the pressure value at the point (0,85,0) mm in the absence of a plate. First column: Pressure amplitudes on $y = 85$ mm axis for different incident angles. Second column: Phases of $y = 85$ mm axis. Third column: Pressure amplitudes on $x = 0$ mm axis for different incident angles. Fourth column: Phases of $x = 0$ mm axis.

LIST OF TABLES

TABLE I

ACOUSTIC PARAMETERS FOR THE PLASTICS AT THE FREQUENCY 531 KHZ

	c (m/s)	ρ (kg/m^3)	α (Np/m)
Water	1498	1000	0
Plastic 1	2185	1187	19.4
Plastic 2	2770	1236	13.7
Rubber	1520	1089	31.7

TABLE II

A SUMMARY OF DIFFERENCES IN SIMULATED AND MODELED FIELDS FOR BOTH PLATES.

	Plate 1		Plate 2	
Rotation θ	Amp. error $\epsilon_{\lvert p\rvert}$ %	Phase error $\epsilon_{\arg p}$ ± SD	Amp. error $\epsilon_{\lvert p\rvert}$ %	Phase error $\epsilon_{\arg p}$ ± SD
0	20.7	$9.1^\circ \pm 6.9^\circ$	11.2	$52.2^\circ \pm 7.2^\circ$
10	9.9	$11.9^\circ \pm 10.2^\circ$	22.8	$17.1^\circ \pm 9.3^\circ$
20	34.3	$16.6^\circ \pm 10.0^\circ$	44.2	$17.6^\circ \pm 11.6^\circ$
30	19.2	$121.1^\circ \pm 22.2^\circ$	70.3	$58.7^\circ \pm 50.0^\circ$